J Adv Ceram

Research Article

Eu^{2+}-actived oxyfluoride glass with highly efficient blue–cyan luminescence for X-ray imaging and white LED applications

Junyu Chen, Yuheng Mei, Huihui Lin, Lianjie Li, Hai Guo✉

Cite this article: Chen J, Mei Y, Lin H, et al. *J Adv Ceram* 2026, **15**(5): 9221286. https://doi.org/10.26599/JAC.2026.9221286

ABSTRACT: Eu^{2+}-doped glass has attracted considerable interest due to its dual functionality in X-ray imaging and white light-emitting diodes (LEDs). However, the amorphous nature of glass restricts the improvement of the luminescent efficiency of Eu^{2+}-doped glass. Here, four strategies, including selecting oxyfluoride glass as the host, regulating optical basicity, introducing appropriate heavy elements, and adding carbon powders as reducing agents, were proposed to prepare Eu^{2+}-doped glass with excellent X-ray excited luminescence (XEL) and efficient blue–cyan photoluminescence (PL). For scintillating performance, the optimal glass exhibits a record-breaking XEL intensity reaching 308% of that of commercial $Bi_4Ge_3O_{12}$. Together with high transmittance (> 80% at 472 nm), linear response to X-ray dose, and low detection limit (6.0 $\mu Gy_{air}/s$), the imaging resolution based on optimal glass reaches 24 lp/mm. For PL performance, the intense blue–cyan light of the optimal glass possesses a high external quantum efficiency of 71.2% and excellent thermal stability (the PL intensity at 423 K is 57.7% of that at room temperature). When combined with the 400-nm chip, the optimal glass effectively fills the cyan gap and elevates the color rendering index of the white LED to 91.8. This work offers valuable guidelines and design principles for improving the XEL and PL performance of Eu^{2+}-doped glass.

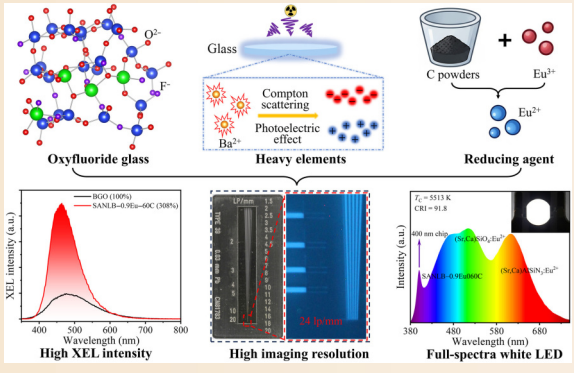

KEYWORDS: Eu^{2+} ion; scintillator; X-ray excited luminescence (XEL); X-ray imaging; full-spectrum lighting

1 Introduction

Luminescent materials are essential components for a wide range of applications, from lighting and display technologies to fundamental scientific research [1–3]. To meet practical demands, luminescent materials need to exhibit high luminescent efficiency, low cost of production, and feasibility of large-scale production [4]. Recently, rare earth (RE) ion-doped glass materials have drawn increasing interest [5,6]. Glass materials offer inherent advantages such as excellent structural stability, compositional tunability, and suitability for producing complex shapes [7]. Among various RE activators, Eu^{2+} ions stand out due to their adjustable emission color, short decay time, and non-toxicity [8]. The luminescence of Eu^{2+} ions originates from the 5d–4f transition, which is allowed by selection rules and is highly susceptible to the surrounding crystal field [9,10]. By modifying the crystal field strength, the luminescent color of Eu^{2+} can be continuously adjusted across the visible light, from blue to red. Owing to these features, Eu^{2+}-doped glass materials have significant potential for advanced optoelectronic applications, including scintillators for X-ray imaging and phosphors for full-spectrum white light-emitting diodes (LEDs).

Scintillators, which are able to transform non-visible X-rays into visible light, function as a critical element within indirect X-ray imaging systems [11,12]. Eu^{2+}-doped glass possesses high transmittance, remarkable X-ray excited luminescence (XEL) intensity, and rapid decay of the scintillating lifetime, making it highly suitable for an appropriate scintillator [13–15]. In addition, the high effective atomic number of Eu^{2+} ions further contributes to the scintillating performance by boosting the absorption efficiency for X-rays [16]. Current research on improving the scintillating performance of Eu^{2+}-doped glass is largely concentrated on the crystallization of glass. For example, we successfully enhanced the XEL intensity of Eu^{2+}-doped glass to 220% of that of commercial $Bi_4Ge_3O_{12}$ (BGO) through precipitation of $Na_5Lu_9F_{32}$:Eu^{2+} nanocrystals [17]. However, scattering effects induced by the nanocrystals inevitably lead to a reduction in the transmittance and imaging resolution [18]. As a result, there is an urgent requirement to develop novel strategies for boosting the XEL intensity of Eu^{2+}-doped glass.

In addition, the luminescence of Eu^{2+} ions in oxyfluoride glass is generally located in the blue–cyan region [19]. Blue–cyan light plays a vital role in filling the cyan gap in full-spectrum white LEDs and improving the color rendering index (CRI) [20,21]. For

Department of Physics, Zhejiang Normal University, Jinhua 321004, China.

✉ Corresponding author. E-mail: ghh@zjnu.cn

Received: January 26, 2026; Revised: March 2, 2026; Accepted: March 19, 2026

© The Author(s) 2026. This is an open access article under the terms of the Creative Commons Attribution 4.0 International License (CC BY 4.0, http://creativecommons.org/licenses/by/4.0/).

instance, Peng *et al.* [22] demonstrated that incorporating $CsPbBr_xCl_{3-x}$ with cyan emission could increase the CRI of commercial white LEDs from 88 to 98. Therefore, Eu^{2+}-doped glass with blue–cyan emission is also well suited for the application of white LEDs. In addition, the superior thermal conductivity and structural stability of Eu^{2+}-doped glass ensure the long-term stable performance of white LEDs.

However, the disordered glass structure restrains the luminescence efficiency of Eu^{2+}-doped glass to some extent. The inherent defects in glass act as quenching centers, promoting nonradiative energy loss and diminishing light output [23]. Therefore, developing Eu^{2+}-doped glass exhibiting highly efficient blue–cyan luminescence remains a significant challenge. Here, a series of strategies is proposed to enhance the XEL and photoluminescence (PL) performance of Eu^{2+}-doped glass. First, oxyfluoride glass was selected as the host material for Eu^{2+} ions, which combines the advantages of both fluoride and oxide glasses. A suitable amount of fluoride in the glass reduces the phonon energy, thereby reducing the probability of nonradiative transitions and enhancing the XEL and PL intensity [24]. Meanwhile, the network structure composed of oxide can provide a stable protective layer for luminescent centers [25]. Second, the luminescent color of Eu^{2+} was adjusted by regulating the optical basicity of the glass. In glass materials, the crystal field strength shows a positive correlation with the optical basicity [26]. By adding appropriate amounts of Na, Li, and Ba to increase the optical basicity, the luminescent color of Eu^{2+} could be adjusted to the desired blue–cyan light [27,28]. Third, the heavy element Ba was added to increase the density and X-ray attenuation coefficient of glass, which facilitates the absorption of X-ray energy [29]. Finally, during the high-temperature melting process of glass, to reduce Eu^{3+} to Eu^{2+}, it is necessary to add reducing agents, such as carbon (C) powders, Al powders, Sb_2O_3, and Si_3N_4. Al powders, Sb_2O_3, and Si_3N_4 introduce extra Al_2O_3, Sb_2O_5, and SiO_2 into glass, which will influence the glass structure and luminescent performance of Eu^{2+}-doped glass [30]. In comparison, C powders reduce Eu^{3+} to Eu^{2+} and are eventually released as CO_2, which has a minimal effect on the glass structure. In addition, using C powders as reducing agents has the advantages of simplicity, cost-effectiveness, and high efficiency. Therefore, in this work, C powders were introduced into raw materials as reducing agents.

To verify the above strategies, a novel Eu^{2+}-doped oxyfluoride glass was prepared, and its multifunctional performance was investigated. For X-ray imaging application, the optimal glass exhibits high transmittance (> 80% at 472 nm), a record-breaking XEL intensity of 308% of that of BGO between Eu^{2+}-doped glass scintillators (Table 1), and an excellent spatial resolution of 24 lp/mm. In addition, even after being immersed in water for 30 d, the imaging quality shows no deterioration due to the excellent physical and chemical stability of the optimal glass. For the full-spectrum white LED, the optimal glass shows a high absorption efficiency (Abs) of 89.3%, external quantum efficiency (EQE) of 71.2%, and thermal stability (the PL intensity at 423 K is 57.7% of that at room temperature). The white LED fabricated by optimal glass delivers a high CRI of 91.8, which is higher than that of a commercial white LED. These results highlight the promising role of Eu^{2+}-doped oxyfluoride glass in advancing X-ray imaging and full-spectrum white LEDs.

2 Experiment

2.1 Preparation of samples

The designed glasses with molar composition of SiO_2–Al_2O_3–Na_2O–NaF–LiF–BaF_2–$xEuF_3$–yC powders (SANLB host (x = 0, y = 0), SANLB–0.9Eu–yC (x = 0.9; y = 0, 50, 55, 60), and SANLB–xEu–60C (x = 0.6, 0.8, 0.9, 1.0; y = 60)) were prepared using the conventional melt quenching method. First, raw materials of SiO_2, Al_2O_3, Na_2CO_3, NaF, LiF, BaF_2, EuF_3, and C powders were weighed according to the stoichiometric ratio. All raw materials were ground in an agate mortar for 20 min and then transferred to a corundum crucible. After being melted at 1520 °C for 1 h, the molten liquid was poured onto a preheated copper plate and pressed by another copper plate. Then, the obtained glass was heat-treated at 500 °C for 3 h to release the internal stress. Finally, the glass was polished to the appropriate size (with a thickness of 2 mm) for optical characterization.

2.2 Fabrication of LEDs

The LED was fabricated by composing commercial chips and phosphors. The commercial 450- and 400-nm chips were purchased from Suzhou Uking Photoelectric Technology Co., Ltd. Commercial $Y_3Al_5O_{12}:Ce^{3+}$ (YAG:Ce) phosphor was purchased from Intematix Co., Ltd. Commercial $(Sr,Ba)_2SiO_4:Eu^{2+}$ and $(Sr,Ca)AlSiN_3:Eu^{2+}$ phosphors were purchased from Shenzhen Looking Long Technology Co., Ltd. The used phosphors were first mixed with epoxy resin in a specific ratio and then coated onto the corresponding chips. Then, the LED was cured at 100 °C for 60 min.

2.3 Characterization

X-ray diffraction (XRD) patterns of the prepared samples were obtained by an X-ray diffractometer (Rigaku MiniFlex/600) equipped with a Cu $K\alpha_1$ radiation source. The transmittance of the samples was measured by an ultraviolet–visible spectrophotometer (Hitachi U-3900). Fourier transform infrared (FTIR) spectra were obtained using an FTIR spectrophotometer (NEXUS 670). PL, photoluminescence excitation (PLE), decay time, and quantum efficiency were characterized by a fluorescence spectrophotometer (Edinburgh FS5) equipped with a xenon lamp light source and a 405-nm pulse laser. The temperature was regulated and monitored by a temperature controller (Techcomp TCB1402C). XEL spectra were recorded by a spectrometer (Zolix OmniFluo960) equipped with an X-ray tube (Moxtek TUB00154-9I-W06). During the measurement process, the dose rate of the X-ray tube was set at 43.0 mGy_{air}/s. For the measurement of XEL spectra based on different dose rates of the X-ray tube, the dose rates of the X-ray tube were set at 1.26–43.0 mGy_{air}/s. The decay

Table 1 Comparison of XEL intensity and imaging resolution among Eu^{2+}-doped and Ce^{3+}-doped scintillators

Sample	XEL	Resolution (lp/mm)	Ref.
LAS:Eu^{2+}	38.6%	—	[31]
$CsCaCl_3:Eu^{2+}$ (GC*)	93%	30.0	[32]
$Ba_2SiO_4:Eu^{2+}$ (GC*)	98%	7.0	[14]
Eu^{2+} glass	120%	—	[33]
$BaCl_2:Eu^{2+}$ (GC*)	132%	20.0	[34]
GEu8Al29	165%	20.0	[35]
$SrMg_2Al_6Si_9O_{30}:Eu^{2+}$ (GC*)	169%	8.0	[15]
G–0.6Eu–2.4Al	169%	20.0	[36]
$K(Y,Gd)F_4:Ce^{3+}$ (GC*)	181%	7.9	[37]
$Na_5Lu_9F_{32}:Eu^{2+}$ (GC*)	220%	23.8	[17]
SANLB–0.9Eu–60C	308%	24.0	This work

Note: GC*: glass ceramics.

time under X-ray irradiation was measured by a picoX 5084 X-ray excitation luminescence lifetime/decay testing system (Shanghai UPU Optoelectronic Technology Co., Ltd.). Temperature-dependent XEL spectra were collected by a custom-built spectral system equipped with a Godzilla fiber spectrometer, a Moxtek TUB00154-9I-W06 X-ray tube, and a JF-956 copper heater. The X-ray images were taken by a custom-built X-ray imaging system equipped with an X-ray tube, a reflector, and a camera (Canon EOS 600D). The thickness of the glass scintillator is 2 mm. The distance between the X-ray source and object was 5 cm, the distance between the object and scintillator was 0 cm, and the distance between the scintillator and camera was 7.5 cm. The exposure time of the camera was set to 5 s. The performance of the prepared LED was evaluated through a photoelectric measurement and analysis system (Everfine ATA-1000 LED).

3 Results and discussion

3.1 Structural characterization

Figure 1(a) and Fig. S1 in the Electronic Supplementary Material (ESM) show the XRD patterns of the SANLB host, SANLB–0.9Eu–0C, SANLB–0.9Eu–60C, and other samples. After the introduction of the EuF_3 and reducing agent C powders, the XRD patterns still show two broad diffraction bands, and no diffraction peaks appear. This indicates that the EuF_3 and C powders do not affect the amorphous structure of the SANLB sample [15]. FTIR spectra of the SANLB host, SANLB–0.9Eu–0C, and SANLB–0.9Eu–60C are recorded in Fig. 1(b). The absorption band peaking at 437 cm^{-1} comes from the bending vibration of Si–O–Si/Al bridge oxygen. In addition, two absorption bands peaking at 707 and 979 cm^{-1} are attributed to the asymmetric stretching vibrations of $[AlO_4]$ and $[SiO_4]$ tetrahedra, respectively [38]. There is no obvious change in the FTIR spectra between the SANLB host, SANLB–0.9Eu–0C, and SANLB–0.9Eu–60C, indicating that the introduction of EuF_3 and C powders has a negligible effect on the glass network structure.

Figure 1(c) exhibits the transmittance spectra of the SANLB host and SANLB–0.9Eu–*y*C. For SANLB–0.9Eu–0C, the absorption peaks at 393 and 465 nm arise from the $^7F_0 \rightarrow {}^5L_6$ and $^5D_2$ transitions of the Eu^{3+} ion, respectively [34]. In addition, compared with the SANLB host, the transmission spectra of SANLB–0.9Eu–0C show an obvious redshift. The strong absorption at 250–450 nm is identified as the 4f–5d transition of Eu^{2+} ions due to self-reduction of Eu^{3+} to Eu^{2+} in the SANLB sample [19]. After adding C powder as a reducing agent, the absorption spectra of SANLB–0.9Eu–*y*C samples further redshift, and the absorption peaks of Eu^{3+} ions disappear. This indicates that C powders can effectively reduce Eu^{3+} to Eu^{2+}. When the concentration of C powders exceeds 60%, the transmittance of SANLB–0.9Eu–65C in the visible light range shows an obvious decline, ascribed to the deposition of excessive C powders. Therefore, during the subsequent optimization process of the concentration of EuF_3, the concentration of C powders was fixed at 60%. Figure 1(d) displays the transmittance spectra of SANLB–*x*Eu–60C. The transmittance of all samples at 472 nm exceeds 80%. High transmittance can effectively reduce light scattering and improve the imaging resolution [39,40]. In addition, the bandgap (E_g) of the SANLB host was calculated based on the Kubelka–Munk function (Fig. S2 in the ESM). The appropriate E_g value of 4.28 eV is beneficial for the luminescent efficiency and thermal stability.

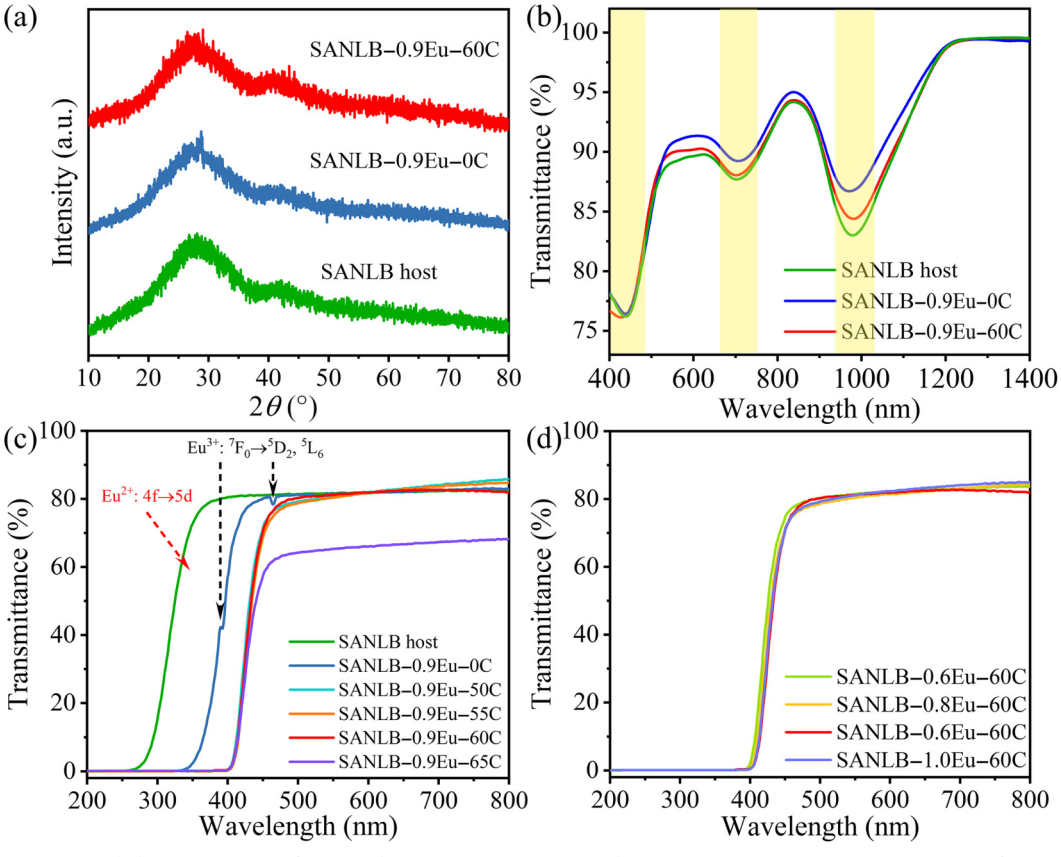

Fig. 1 (a) XRD patterns and (b) FTIR spectra of SANLB host, SANLB–0.9Eu–0C, and SANLB–0.9Eu–60C; transmittance spectra of (c) SANLB host and SANLB–0.9Eu–*y*C, and (d) SANLB–*x*Eu–60C.

清華大学出版社 Tsinghua University Press | SciOpen

3.2 Photoluminescent properties

Figure 2(a) and Fig. S3 in the ESM reveal the PLE (λ_{em} = 472 nm) and PL (λ_{ex} = 401 nm) of SANLB–0.9Eu–*y*C. The broad PLE band in the range of 250–460 nm is attributed to the 4f–5d transition of Eu^{2+} ions [17], which is consistent with the absorption of Eu^{2+} shown in Fig. 1(c). Under the excitation by 401 nm light, the weak PL peaks at 590, 614, 653, and 701 nm are ascribed to $^5D_0 \rightarrow {}^7F_{1,2,3,4}$ transitions of Eu^{3+} ions, respectively [34]. The broad PL band in the range of 425–700 nm corresponds to the 5d–4f transition of Eu^{2+} [36]. After adding C powder as a reducing agent, the PL intensity of Eu^{2+} is enhanced, while the PL of Eu^{3+} disappears. This indicates that C powders can effectively reduce Eu^{3+} to Eu^{2+} and thereby enhance the PL intensity of Eu^{2+} ions. The optimal concentration of C powders for the PL of SANLB–0.9Eu–*y*C is 60%. Figure 2(b) demonstrates the PLE (λ_{em} = 472 nm) and PL (λ_{ex} = 401 nm) of SANLB–*x*Eu–60C. With increasing EuF_3 concentration, the PL intensity of Eu^{2+} first increases and then decreases because of the concentration quenching effect. The optimal sample is obtained when the concentration of EuF_3 is 0.9%. The internal quantum efficiency (IQE), EQE, and Abs of the optimal SANLB–0.9Eu–60C sample were measured and are displayed in Fig. 2(c). The detailed calculational methods are provided in Section S4 in the ESM. SANLB–0.9Eu–60C shows a high EQE of 71.2% and a high Abs of 89.3%, demonstrating its potential for application as a white LED. In addition, based on Duffy's empirical formula [41], the optical basicity of SANLB was calculated to be 0.573. The appropriate optical basicity results in blue–cyan emission of Eu^{2+} ions in SANLB glass.

Figure 2(d) and Fig. S4 in the ESM record the fluorescence decay curves (λ_{em} = 472 nm, λ_{ex} = 405 nm) of SANLB–0.9Eu–*y*C and SANLB–*x*Eu–60C, respectively. The lifetime (τ) of the 5d level of Eu^{2+} was evaluated based on Eq. (1) [42]:

$$\tau = \int tI(t)\mathrm{d}t / \int I(t)\mathrm{d}t \quad (1)$$

where t and $I(t)$ are the time and PL intensity, respectively. The values of τ of SANLB–0.9Eu–*y*C are 0.81, 1.71, 1.20, and 1.21 μs, respectively. After adding C powder as a reducing agent, the concentration of Eu^{2+} ions increases, while the concentration of Eu^{3+} ions decreases. This inhibits the energy transfer from Eu^{2+} to Eu^{3+} and prolongs the τ of Eu^{2+}. The energy transfer from Eu^{2+} to Eu^{3+} in the SANLB sample is further verified by the spectral overlap between the PL of Eu^{2+} and PLE of Eu^{3+} (Fig. S5 in the ESM). The values of τ of SANLB–*x*Eu–60C are 1.24, 1.22, 1.21, and 1.19 μs, respectively. As the concentration of Eu^{2+} increases, the shorter distance between Eu^{2+} ions increases the probability of nonradiative relaxation, resulting in a slight decrease in the τ of Eu^{2+}. In addition, the τ of Eu^{2+} in SANLB samples falls within the microsecond range, which is conducive to static X-ray imaging. Figure 2(e) describes the temperature-dependent PL spectra of optimal SANLB–0.9Eu–60C. With increasing temperature, the PL intensity of Eu^{2+} decreases gradually. As shown in Fig. 2(f), when the temperature rises to 423 K, the PL intensity of SANLB–0.9Eu–60C remains 57.7% of that at room temperature. In addition, during the 5 cycles of heating and cooling experiments (Fig. S6 in the ESM), the PL intensity of Eu^{2+} can recover to its initial level. High thermal stability and repeatability benefits for the long-term application of white LEDs.

3.3 Scintillating properties

Figure 3(a) provides the X-ray absorption coefficients of SANLB–0.9Eu–60C, BGO, Si, and YAG:Ce based on the National Institute of Standards and Technology XCOM: Photon cross sections database. In contrast, the X-ray absorption coefficient of SANLB–0.9Eu–60C is higher than that of Si, comparable to that of commercial YAG:Ce, while lower than that of BGO. Figure 3(b) plots the attenuation efficiency of SANLB–0.9Eu–60C varying with thickness. When the thickness of SANLB–0.9Eu–60C is 2 mm, its attenuation efficiency for X-rays can reach 99.3%, demonstrating a strong ability to absorb X-rays.

To characterize the XEL intensity of the designed glass samples,

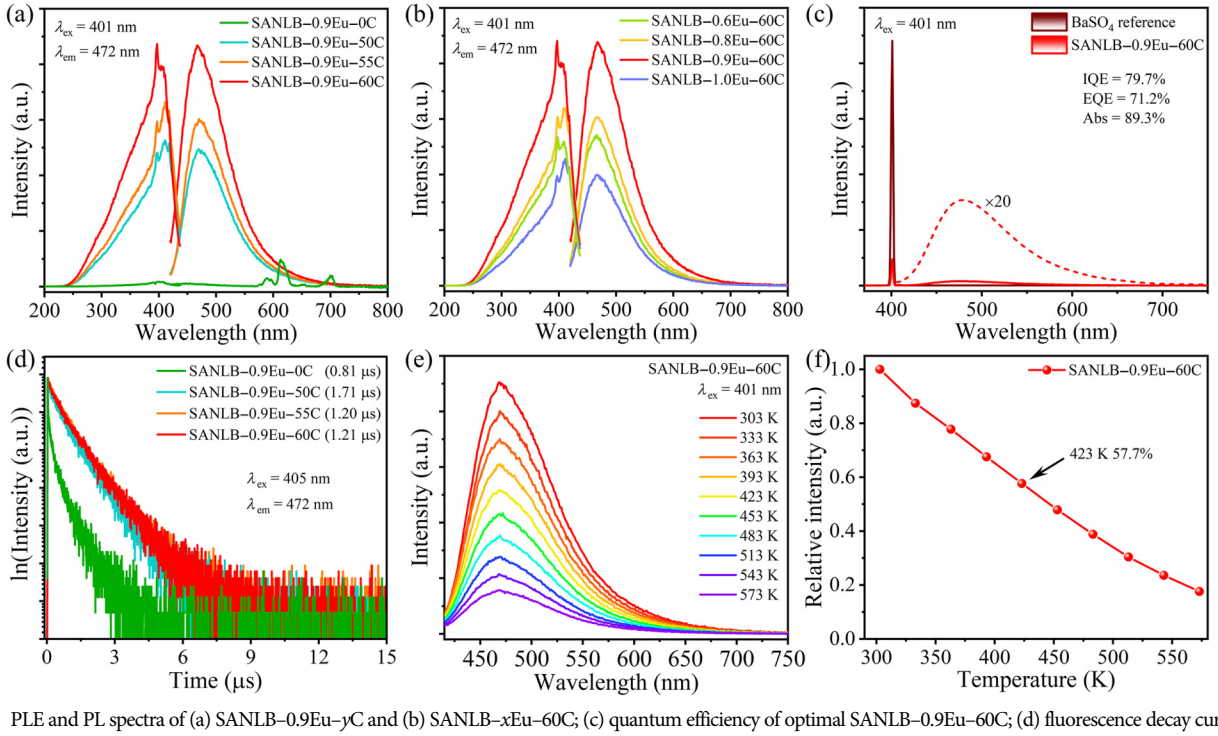

Fig. 2 PLE and PL spectra of (a) SANLB–0.9Eu–*y*C and (b) SANLB–*x*Eu–60C; (c) quantum efficiency of optimal SANLB–0.9Eu–60C; (d) fluorescence decay curves of SANLB–*x*Eu–60C; (e) temperature-dependent PL spectra of SANLB–0.9Eu–60C; and (f) corresponding relative PL intensity varying with temperature.

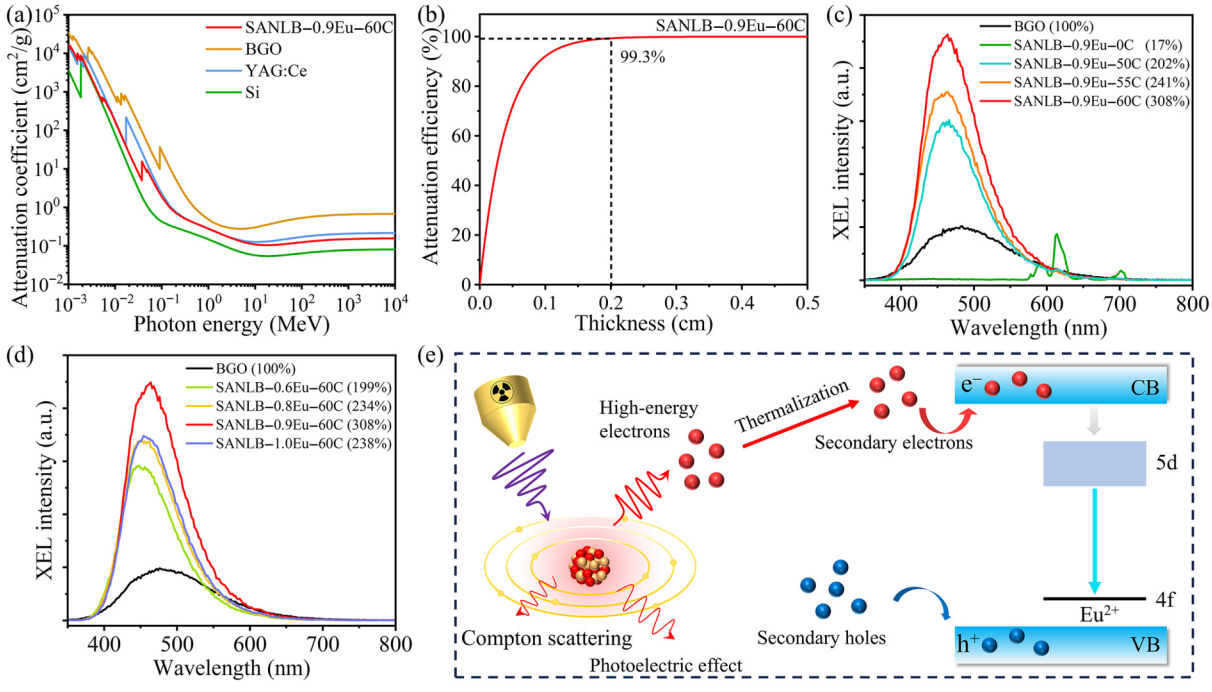

Fig. 3 (a) X-ray absorption coefficients of SANLB–0.9Eu–60C, BGO, YAG:Ce, and Si; (b) attenuation efficiency of SANLB–0.9Eu–60C varying with thickness; XEL spectra of (c) SANLB–0.9Eu–*y*C and (d) ANLB–*x*Eu–60C; (e) mechanism of XEL in SANLB–0.9Eu–60C.

Figs. 3(c) and 3(d) compare the XEL spectra of SANLB–0.9Eu–*y*C and SANLB–*x*Eu–60C with BGO, respectively. The highest XEL intensity is obtained in SANLB–0.9Eu–60C, which reaches 308% of that of BGO. Such excellent XEL intensity is higher than that in most reported Eu^{2+}-doped and Ce^{3+}-doped scintillators listed in Table 1. In detail, the broadband XEL peak at 472 nm corresponds to the 5d–4f transition of the Eu^{2+} ion, and the XEL peaks at 590, 614, 653, and 701 nm are ascribed to the $^5D_0 \rightarrow {}^7F_{1,2,3,4}$ transitions of Eu^{3+} [43]. After adding C powder as a reducing agent, the XEL of Eu^{3+} disappears, while the XEL intensity of Eu^{2+} ions is significantly enhanced, which is consistent with the PL spectra (Fig. 2(a)). In addition, as shown in Fig. 3(d), the XEL intensity of Eu^{2+} first increases and then decreases due to the concentration quenching effect. The excellent scintillating performance of SANLB–0.9Eu–60C can be elaborated from the following aspects. First, the low phonon energy of the oxyfluoride glass host enhances the luminescence of Eu^{2+}. Second, C powders effectively reduce Eu^{3+} to Eu^{2+}. On the basis of reasonable optimization of the EuF_3 and C powder concentrations, excellent luminescent efficiency of Eu^{2+} was obtained. Third, the high transparency of Eu^{2+}-doped glass helps to effectively output light. The lifetime of SANLB–0.9Eu–60C under X-ray irradiation was calculated to be 1.61 μs (Fig. S7 in the ESM). SANLB–0.9Eu–60C, with a relatively long lifetime, could be used for static X-ray imaging.

The mechanism of XEL in SANLB–0.9Eu–60C is revealed in Fig. 3(e). First, the incident X-ray mainly interacts with heavy ions in glass, such as Ba^{2+} and Eu^{2+}. This process will generate a large number of high-energy electrons and holes through the photoelectric effect and Compton scattering. Subsequently, high-energy electrons and holes are transformed into low-energy secondary electrons and holes through thermalization. Then, these secondary electrons are absorbed by the Eu^{2+} ion, exciting it from the 4f ground state to the 5d excited state. The electrons at the 5d excited state of Eu^{2+} finally radiate to the 4f ground state, resulting in strong and broad emission located in the blue–cyan light region.

In addition to its excellent XEL intensity, the radiation resistance of optimal SANLB–0.9Eu–60C under an extreme irradiation environment was further investigated. Figure 4(a) presents the XEL spectra of SANLB–0.9Eu–60C under continuous X-ray irradiation, with measurements taken at 5-min intervals. With increasing irradiation time, the shape and position of the XEL spectra do not undergo any obvious changes, but the XEL intensity increases gradually due to the bright burn effect. During the first 30 min, Eu^{2+} ions compete with traps for the absorption of carriers. As traps are gradually filled, Eu^{2+} can absorb more carriers and generate stronger XEL [44,45]. As shown in Fig. 4(b), after X-ray irradiation for 30 min, the XEL intensity of SANLB–0.9Eu–60C increases to 115% of the initial value and then remains stable. In addition, after heat treatment at 300 °C for 1 h, the XEL intensity of SANLB–0.9Eu–60C could be restored to the initial level (Fig. S8 in the ESM). Figure 4(c) shows the transmittance spectra of SANLB–0.9Eu–60C before and after X-ray irradiation. After continuous X-ray irradiation for 100 min, the transmittance of SANLB–0.9Eu–60C does not decrease, indicating the absence of irradiation damage. In addition, after 30 on/off cycles of X-ray excitation (Fig. 4(d)), the XEL intensity of SANLB–0.9Eu–60C remains almost unchanged. Figure S9 in the ESM shows the temperature-dependent XEL spectra and corresponding XEL intensity of SANLB–0.9Eu–60C at 303–573 K. With increasing temperature, the XEL intensity of SANLB–0.9Eu–60C decreases monotonically. The XEL intensity of SANLB–0.9Eu–60C at 423 K is 52.4% of that at 303 K.

In addition to excellent stability under X-ray irradiation, the stability of scintillators in harsh chemical environments is also of crucial importance. To verify this, the SANLB–0.9Eu–60C sample was immersed in air, water, and ethanol for 30 d. Every 5 d, the XEL spectra of SANLB–0.9Eu–60C were measured, and the change in relative XEL intensity is revealed in Fig. 4(e). The XEL intensity of SANLB–0.9Eu–60C exhibits almost no decrease after a long period of immersion. The high stability is mainly attributed to the chemically stable protective layer provided by the oxyfluoride glass host for the luminescence centers. Figure S10 in

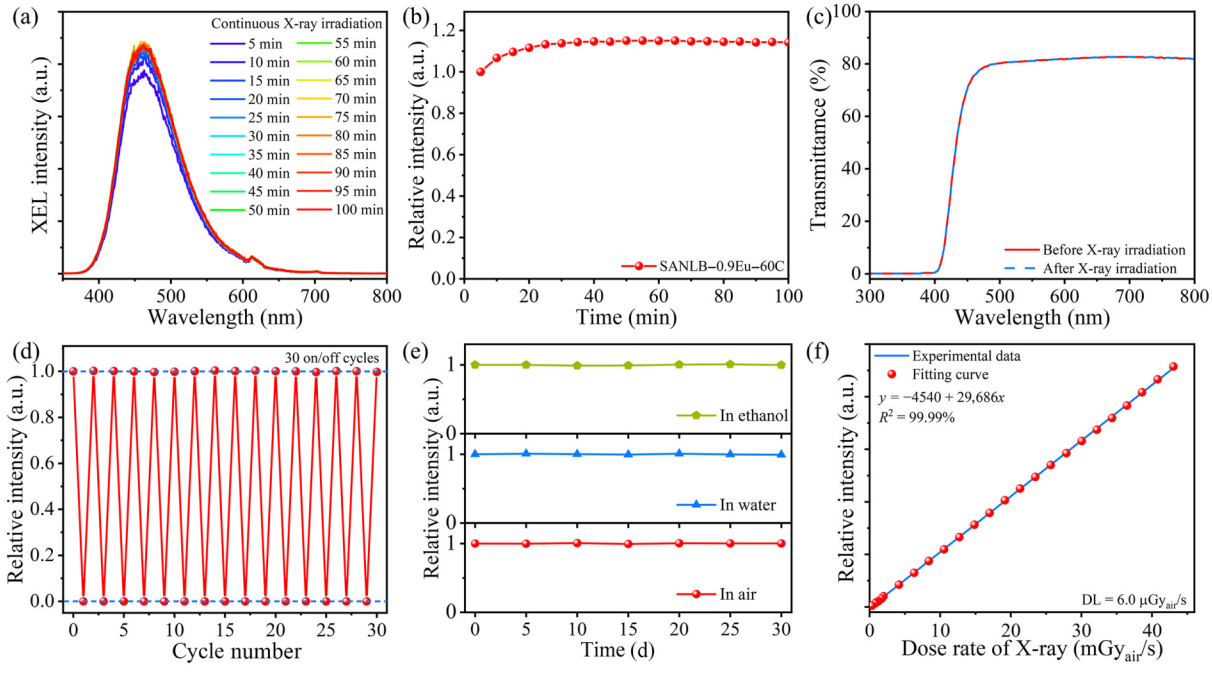

Fig. 4 (a) XEL spectra and (b) corresponding relative intensity of SANLB–0.9Eu–60C under continuous X-ray irradiation; (c) transmission spectra of SANLB–0.9Eu–60C before and after X-ray irradiation; (d) XEL intensity recorded for SANLB–0.9Eu–60C over 30 on/off cycles; (e) relative XEL intensity of SANLB–0.9Eu–60C immersed in air, water, and ethanol for 30 d; (f) XEL intensity of SANLB–0.9Eu–60C under X-ray irradiation at different dose rates.

the ESM shows the XEL intensity of SANLB–0.9Eu–60C under X-ray irradiation at different dose rates. As the dose rate of X-ray tube increases, the XEL intensity of SANLB–0.9Eu–60C increases gradually. Figure 4(f) plots the fitted linear curve between the XEL intensity and the dose rate of X-ray tube. A high correlation coefficient (99.99%) indicates a sensitive response of SANLB–0.9Eu–60C to X-rays, which is beneficial for X-ray imaging resolution [46]. In addition, the limit of detection (DL) of SANLB–0.9Eu–60C was assessed to be 6.0 $\mu Gy_{air}/s$. Low DL can effectively reduce damage to tissues during medical imaging.

3.4 X-ray imaging

The X-ray imaging performance of SANLB–0.9Eu–60C was investigated by a homemade X-ray imaging system (Fig. 5(a)). Figure 5(b) shows photographs and corresponding X-ray images of the chip and seed. The X-ray images clearly reveal the internal features of imaging objects. The imaging quality of a scintillator is generally characterized by the imaging resolution, which can be measured by a standard X-ray test pattern [47]. Figure 5(c) demonstrates the photograph and corresponding X-ray image of the standard X-ray test pattern. As shown in Fig. S11 in the ESM, the ends of the light and dark stripes can be clearly distinguishable, which hinders the imaging resolution of SANLB–0.9Eu–60C to 24 lp/mm (Fig. S12 in the ESM). In addition, the modulation transfer function (MTF) was calculated to quantitatively evaluate the imaging performance of SANLB–0.9Eu–60C. As shown in Fig. 5(d), when MTF equals 0.2, the resolution of SANLB–0.9Eu–60C is determined to be 25.1 lp/mm, which is consistent with visual observations. The imaging resolution is higher than that of most reported Eu^{2+}- and Ce^{3+}-doped scintillators listed in Table 1.

To evaluate the underwater imaging ability of SANLB–0.9Eu–60C, the SANLB–0.9Eu–60C and imaging objects were both immersed in water for 30 d. Every 5 d, X-ray images of the chip were taken and are displayed in Fig. 5(f). Meanwhile, the average gray values of these images were calculated (Fig. 5(g)) to monitor the stability of brightness. The clarity and brightness of the X-ray image remain highly stable over the 30-d immersion period. This is attributed to the excellent physical and chemical stability provided by oxyfluoride glass. In addition, the underwater X-ray image of the standard X-ray test pattern (Fig. S13 in the ESM) indicates that the underwater imaging resolution of SANLB–0.9Eu–60C can also reach 24 lp/mm. Compared with other reported scintillators for underwater X-ray imaging (Table S1 in the ESM), SANLB–0.9Eu–60C shows higher underwater imaging performance. These findings demonstrate the significant potential of the SANLB–0.9Eu–60C scintillator for prolonged underwater imaging application.

3.5 Full-spectrum white LED

The typical commercial white LED is composed of a 445-nm chip emitting blue light and a YAG:Ce phosphor emitting yellow light (labeled LED#1). As shown in Fig. 6(a), the emitting color of LED#1 falls within the range of white light (Fig. S14(b) in the ESM), but it has shortcomings such as blue overshoot, cyan gap, and red loss. These shortcomings lead to a relatively low CRI of 71.6 and a high correlated color temperature (CCT, T_c) of 10,168 K. SANLB–0.9Eu–60C with strong blue–cyan emission can replace the blue light chip and fill the cyan gap. Figure S14(a) in the ESM presents the emission spectra of an LED composed of a 400-nm chip and a SANLB–0.9Eu–60C sample (labeled LED#2). The weak peak at 400 nm comes from the emission of the 400-nm chip. The broad emission located in the range of blue–cyan (Fig. S14(b) in the ESM) originates from the SANLB–0.9Eu–60C sample, which is consistent with the PL spectra of SANLB–0.9Eu–60C (Fig. 2(b)).

Subsequently, commercial $(Ba,Sr)_2SiO_4:Eu^{2+}$ with green light emission and $(SrCa)AlSiN_3:Eu^{2+}$ with red light emission were mixed with the SANLB–0.9Eu–60C sample and then combined with a 400-nm chip to achieve a full-spectrum white LED (labeled as LED#3). LED#3 exhibits continuous emission spectra in the range of visible light, as depicted in Fig. 6(b). The inset of the

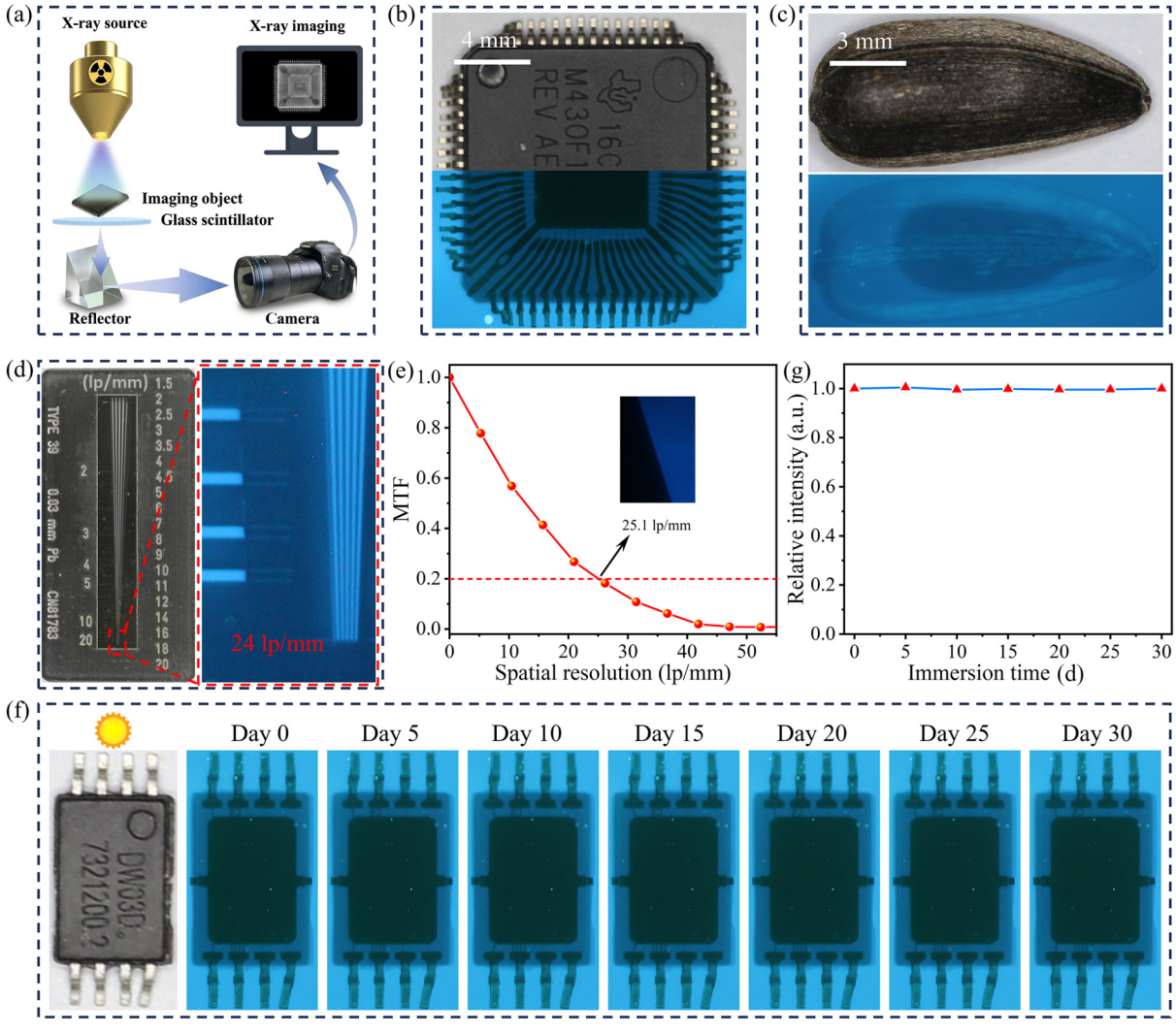

Fig. 5 (a) Homemade X-ray imaging system; photographs and corresponding X-ray images of (b) chip, (c) seed, and (d) standard X-ray test pattern plate based on SANLB–0.9Eu–60C; (e) calculated MTF curve of SANLB–0.9Eu–60C; (f) photograph and underwater X-ray images of chip immersed in water for 30 d; (h) average gray values of underwater X-ray images.

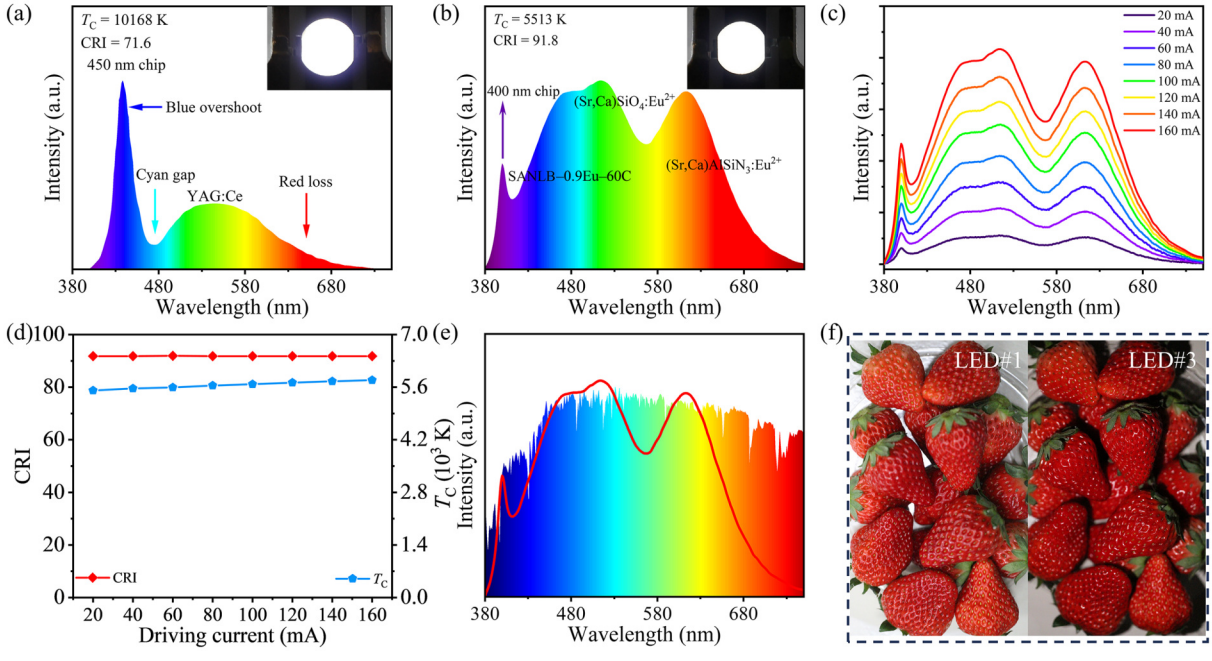

Fig. 6 Emission spectra and corresponding photographs of (a) LED#1 and (b) LED#3; (c) emission spectra and (d) corresponding CRI and T_C of LED#3 under different driving currents; (e) comparison of emission spectra of LED#3 and solar light; (f) comparison of images of strawberries illuminated by LED#1 and LED#3.

清華大学出版社 Tsinghua University Press | SciOpen

device photograph and the CIE chromaticity diagram (Fig. S14(b) in the ESM) both manifest successful generation of white illumination. In contrast to LED#1, LED#3 effectively reduces blue light, fills the cyan gap, and compensates for the red loss, yielding a higher CRI of 91.8 and a lower CCT of 5513 K. Figure 6(c) records the emission spectra of LED#3 under driving currents ranging from 20 to 160 mA. Although the emission intensity increases with rising current, the spectral shape and peak positions remain stable. With increasing driving current, the CRI of LED#3 shows no significant variation, and the CCT of LED#3 shows a slight increase (Fig. 6(d)). In addition, Fig. 6(e) indicates that the emission spectra of LED#3 closely resemble those of natural sunlight. A comparison of LED#3 and LED#1 (Fig. 6(f)) reveals that strawberries illuminated by LED#3 exhibit more natural and realistic color rendition. These findings collectively demonstrate that SANLB–0.9Eu–60C is a highly promising blue–cyan emitting phosphor suitable for high-quality and full-spectrum white LEDs.

4 Conclusions

By employing oxyfluoride glass as the host material, regulating optical basicity, and introducing the heavy element Ba^{2+} along with reduction by C powders, the blue–cyan PL and XEL performance of Eu^{2+}-doped glass is significantly enhanced. The optimal SANLB–0.9Eu–60C glass exhibits high transmittance (> 80% at 472 nm), excellent EQE of 71.2%, and record-breaking XEL intensity of 308% of that of BGO. For X-ray imaging application, the spatial resolution of SANLB–0.9Eu–60C can reach 24 lp/mm. In addition, high radiation resistance and excellent environmental stability ensure the feasibility of long-term underwater imaging. For the full-spectrum white LED, the strong blue–cyan emission of SANLB–0.9Eu–60C fills the cyan gap of the commercial white LED. The white LED fabricated using SANLB–0.9Eu–60C shows a high CRI of 91.8 and a low CCT of 5513 K. These results suggest that the designed SANLB–0.9Eu–60C is a promising candidate for applications in X-ray imaging and white LED technologies.

Acknowledgements

This work was supported by the National Natural Science Foundation of China (No. 12574443).

Author contributions

Junyu Chen: investigation, writing – original draft; Yuheng Mei: investigation, writing – original draft Huihui Lin: investigation, writing – original draft; Lianjie Li: writing – original draft; Hai Guo: conceptualization, resources, writing – review & editing, supervision.

Availability of data and materials

The data that support the findings of this study are available from the corresponding author upon reasonable request.

Competing interests

The authors have no competing interests to declare that are relevant to the content of this article.

Electronic Supplementary Material

Supplementary material is available in the online version of this article at https://doi.org/10.26599/JAC.2026.9221286.

References

[1] Ou XY, Qin X, Huang BL, *et al.* High-resolution X-ray luminescence extension imaging. *Nature* 2021, **590**: 410–415.

[2] Kim JS, Heo JM, Park GS, *et al.* Ultra-bright, efficient and stable perovskite light-emitting diodes. *Nature* 2022, **611**: 688–694.

[3] Yang ZY, de Boer T, Braun PM, *et al.* Thermally stable red-emitting oxide ceramics for laser lighting. *Adv Mater* 2023, **35**: 2301837.

[4] Hariyani S, Sójka M, Setlur A, *et al.* A guide to comprehensive phosphor discovery for solid-state lighting. *Nat Rev Mater* 2023, **8**: 759–775.

[5] Prediger R, Kluck S, Hambitzer L, *et al.* High-precision 3D doping of fused silica glass derived from nanocomposites. *Adv Mater* 2025, **37**: e11245.

[6] Zhu SY, Jin SL, Zhan LK, *et al.* Glass network engineering of yellow-emitting $Ba_2Sc_2B_4O_{11}:Ce^{3+}$ glass ceramics for full-spectrum lighting. *J Adv Ceram* 2025, **14**: 9221169.

[7] Wang DZ, Zhang SY, Chen JF, *et al.* Transparent glass composite scintillator with high crystallinity for efficient thermal neutron detection. *Adv Funct Mater* 2024, **34**: 2401992.

[8] Wang YH, Li ZB, Xue MR, *et al.* Recent progress in Eu^{2+} activated red phosphors for white LEDs and laser displays: Focusing on efficient host screening and innovative structural design. *Coordin Chem Rev* 2026, **546**: 217060.

[9] Pritzl RM, Pointner MM, Witthaut K, *et al.* Tunable narrow-band cyan-emission of Eu^{2+}-doped nitridomagnesophosphates $Ba_{3-x}Sr_x[Mg_2P_{10}N_{20}]:Eu^{2+}$ (x = 0–3). *Angew Chem Int Edit* 2024, **63**: 202403648.

[10] Li L, Jin JC, Han K, *et al.* Rational design and synthesis of narrow-band emitting Eu(II)-based hybrid halides via alkyl thermal cleavage. *Nat Commun* 2025, **16**: 7479.

[11] Kim YC, Kim KH, Son DY, *et al.* Printable organometallic perovskite enables large-area, low-dose X-ray imaging. *Nature* 2017, **550**: 87–91.

[12] Zhang H, Huang XJ, Wan TZ, *et al.* Integrated copper-halide activated scintillator fiber array for remote high-resolution X-ray imaging. *Nat Commun* 2025, **16**: 5973.

[13] Wang DZ, Li HW, Chen JF, *et al.* Congruent glass composite scintillator for efficient high-energy ray detection. *Adv Mater* 2025, **37**: 2412661.

[14] Huang JQ, Yi XD, Gao Y, *et al.* Kinetics-controlled crystallization unlocking Eu^{2+}-doped barium silicate glass ceramic for efficient X-ray scintillation. *Small Methods* 2025, **9**: 01310.

[15] Hu T, Guo YL, Yi XD, *et al.* Integrated multi-responsive $SrMg_2Al_6Si_9O_{30}:Eu^{2+}$ osumilite glass ceramic via *in situ* crystallization: A unified platform for smart optical applications. *Adv Funct Mater* 2026, **36**: 31457.

[16] Li HJ, Li Y, Zhang L, *et al.* A thermo-responsive MOFs for X-ray scintillator. *Adv Mater* 2024, **36**: 2405535.

[17] Pan JW, Lei JH, Wei RF, *et al.* Eu^{2+}-doped transparent glass-ceramics with superior scintillation performance and stability for high-resolution X-ray imaging. *Laser Photonics Rev* 2026, **20**: 01906.

[18] Xu XW, Xie YM, Shi HY, *et al.* Light management of metal halide scintillators for high-resolution X-ray imaging. *Adv Mater* 2024, **36**: 2303738.

[19] Cui JZ, Wen YF, Chen RC, *et al.* Bright cyan emission from Eu-Doped borosilicate glasses by optimizing reduction of Eu^{3+} to Eu^{2+} in ambient atmosphere. *Chem Eng J* 2024, **489**: 151416.

[20] Gao H, Wu HJ, Zhang LL, *et al.* An efficient broadband cyan phosphor for full-spectrum pc-WLEDs. *Laser Photonics Rev* 2025, **19**: 00990.

[21] Ge YP, Zhao M, Zhao YF, *et al.* Tailoring of blue–cyan luminescence in $Rb_3Y[(P_{1-x}Si_x)O_4]_2:Eu^{2+}$ phosphor via Si^{4+}–P^{5+} heterovalent substitution for full-spectrum healthy lighting. *Laser Photonics Rev* 2025, **19**: 2500026.

[22] Peng M, Sun SB, Xu B, *et al.* Polymer-encapsulated halide perovskite color converters to overcome blue overshoot and cyan gap of white light-emitting diodes. *Adv Funct Mater* 2023, **33**: 2300583.

[23] Zhao JT, Fan ZH, Zhou S, *et al.* Defect assisted multicolor luminescence in borosilicate photonic glass for high-level

anticounterfeiting and X-ray imaging. *Adv Funct Mater* 2025, **35**: 2503714.

[24] Wang SK, Yang JD, Liu C, *et al.* $KTb_{3-x}Gd_xF_{10}$ nano-glass composite scintillator with excellent thermal stability and record X-ray imaging resolution. *Laser Photonics Rev* 2025, **19**: 2401611.

[25] Li LJ, Chen JY, He GL, *et al.* Achieving anti-thermal-quenching in Tb^{3+}-doped glass scintillators via dual-channel thermally enhanced energy transfer. *J Adv Ceram* 2026, **15**: 9221220.

[26] Farias AM, Sandrini M, Viana JRM, *et al.* Emission tunability and local environment in europium-doped OH^--free calcium aluminosilicate glasses for artificial lighting applications. *Mater Chem Phys* 2015, **156**: 214–219.

[27] Wang C, Peng MY, Jiang N, *et al.* Tuning the Eu luminescence in glass materials synthesized in air by adjusting glass compositions. *Mater Lett* 2007, **61**: 3608–3611.

[28] Zhao MJ, Tao YT, Wang PT, *et al.* Electron paramagnetic resonance and luminescence properties of Eu^{2+} in oxyfluoride barium borate glasses. *Ceram Int* 2024, **50**: 1857–1866.

[29] Sui ZX, Qian S, Niu LY, *et al.* Glass scintillator: A window to future high-energy radiation detection. *Innovation* 2025, **6**: 100878.

[30] Guo JJ, Chen JY, Li LJ, *et al.* Ce^{3+}-doped $Sr_{0.84}(Lu,Gd)_{0.16}F_{2.16}$ glass-ceramics scintillators for high resolution X-ray imaging. *J Rare Earth* 2025: 10.1016/j.jre.2025.07.003.

[31] Zhu YW, Tang G, Hua ZH, *et al.* Color tunable emission and scintillation properties of Eu-doped lanthanum alumino–silicate glasses. *J Rare Earths* 2025, **43**: 2385–2394.

[32] Zhang YD, Li K, Niu LY, *et al.* Eu^{2+} doped cesium alkaline earth chloride nanocrystals in glass for X-ray imaging. *Ceram Int* 2024, **50**: 31673–31679.

[33] Chewpraditkul W, Shen Y, Chen DP, *et al.* Luminescence of Ce^{3+}- and Eu^{2+}-doped silica glasses under UV and X-ray excitation. *J Optoelectron Adv M* 2013, **15**: 94–98.

[34] Liu QH, Ran P, Chen WL, *et al.* Bright transparent scintillators with high fraction $BaCl_2$: Eu^{2+} nanocrystals precipitation: An ionic-covalent hybrid network strategy toward superior X-ray imaging glass-ceramics. *Adv Sci* 2023, **10**: 2304889.

[35] Zou JH, Li LJ, Chen JY, *et al.* Eu^{2+}-doped oxyfluoride glass scintillator for X-ray imaging. *J Alloy Compd* 2025, **1020**: 179428.

[36] Li LJ, Zou JH, Chen JY, *et al.* Eu^{2+} doped glass scintillators with high-scintillating performances for X-ray imaging. *Mater Today Chem* 2025, **46**: 102724.

[37] Luo CX, Jing Y, Hua ZH, *et al.* Band gap and defect engineering enhanced scintillation from Ce^{3+}-doped nanoglass containing mixed-type fluoride nanocrystals. *ACS Appl Mater Inter* 2023, **15**: 46226–46235.

[38] He GL, Li LJ, Chen JY, *et al.* A thermal stable multi-functional Cu^+-doped glass for high-resolution X-ray imaging and full-spectra lighting. *Laser Photonics Rev* 2025, **19**: 00396.

[39] Zhao CH, Wang YZ, Bao SY, *et al.* High-performance hybrid organic-inorganic lanthanide halide glass scintillators enabled by dehydration for efficient X-ray imaging. *Adv Mater* 2025, **37**: 2500925.

[40] Wang T, Hu S, Ji T, *et al.* High-temperature X-ray imaging with transparent ceramics scintillators. *Laser Photonics Rev* 2024, **18**: 2300892.

[41] Shi YF, Wei RF, Guo JL, *et al.* Influence of optical basicity on Cu^+ luminescence in aluminosilicate oxyfluoride glasses. *Front Mater* 2019, **6**: 246.

[42] He GL, Chen JY, Li LJ, *et al.* Cu^+-doped oxyfluoride glass with anti-thermal-quenching luminescence for X-ray imaging and WLED. *J Adv Ceram* 2025, **14**: 9221116.

[43] Zhao M, Ge YP, Li YR, *et al.* Achieving Eu^{2+} luminescence at trivalent lattice site in $Rb_3Y(PO_4)_2$:Eu toward multicolor emissions by carbon and hydrogen coreduction. *Adv Funct Mater* 2025, **35**: 2412480.

[44] Průša P, Kučera M, Vedda A, *et al.* Substantial reduction of trapping by Mg co-doping in LuAG:Ce, Mg epitaxial garnet films. *J Lumin* 2021, **238**: 118230.

[45] Rodriguez MG, Denis G, Akselrod MS, *et al.* Thermoluminescence, optically stimulated luminescence and radioluminescence properties of Al_2O_3:C,Mg. *Radiat Meas* 2011, **46**: 1469–1473.

[46] Deng YJ, Xu YK, Qian CY, *et al.* Manganese halide-based glass-ceramic scintillator for ultra-stable and multi-functional X-ray imaging in extreme environments. *Laser Photonics Rev* 2025, **19**: 01178.

[47] Pang T, Lin SS, You FL, *et al.* Synergistic enhancement of crystallinity and transparency in Tb^{3+}-doped nano-glass-ceramics for high-resolution X-ray imaging. *J Adv Ceram* 2025, **14**: 9221122.